Simulation of tectonic stress field and prediction of tectonic fractures in shale reservoirs: A case study of the Ansai area in the Ordos Basin, China

Yunfei Wu[1], Chenglin Liu[1], Qibiao Zang[1], Rizwan Sarwar Awan[1], Guoxiong Li[1], Yuping Wu[1], Xiya Yang[1], and Zhendong Lu[1]

Abstract

The Chang 7 oil-bearing layers from the Ansai area of the Ordos Basin are abundant in oil and gas resources. These layers are chiefly comprised of shales interbedded with tight sandstone. In the regions where the exploration level is relatively low and the structures are gentle in the Ansai area, the distribution of fractures in shale reservoirs and tight sandstone reservoirs is significant for predicting sweet spots and determining the success rate of hydraulic fracturing. In this research, the results acquired from the scanning electron microscope (SEM), cores, thin sections, and image logging determined the developmental characteristics of fractures. Moreover, the Himalayan stress field was modeled using ANSYS, whereas the two-factor method is used to predict the distribution of tectonic fracture by combining stress field and fracture criterion. The results indicate a gradually decreasing trend of the maximum principal stress from east to west. The minimum principal stress in the western part is less than that in the eastern part. The differential stress that can indicate the degree of tectonic deformation ranges from 17 Mpa to 25 MPa. The fracture density ranges from 0 strip/m to 1.5 strip/m. In addition, the areas with more fractures are mainly located in the western and southeastern parts, where shale oil is relatively rich. Similarly, the comparison of different maps illustrates that the distribution of tectonic fracture is related to mechanical parameters and stress fields.

Introduction

Unconventional oil and gas have made great breakthroughs in the Sichuan Basin, the Songliao Basin, and the Ordos Basin in China (Cui et al., 2019). The shale thickness from the Chang 7 oil-bearing layers of the Ansai area is 4–10 m. This area is widely distributed and extended to approximately 2.22×10^8 km^2. The shale with abundant organic matter and high maturity is a good source rock and is considered to be an unconventional reservoir. Liu et al. (2018b) determine that the resource potential of shale oil is approximately 4.42×10^8 m^3, which indicates that the Chang 7 has a great exploration and development potential. Natural fractures act as effective storage space and seepage channels for oil and gas in shale reservoirs and tight sandstone reservoirs. Moreover, during the development of fractures in horizontal wells, the natural fractures after fracturing are closely related to the performance of the reservoir. Therefore, fracture prediction is very important in those areas where the degree of exploration is relatively low. It is helpful for effectively predicting the sweet spots and provides an important basis for fracture development in horizontal wells. Many scholars have studied the fractures of the Yanchang Formation in the Ordos Basin, whereas the fracture prediction of Chang 7 reservoir in the Ansai area has not been conducted. Specifically, Zeng et al. (2007) study the fractures of the Yanchang Formation from the Ordos Basin and find that the occurrence of fractures is mainly related to the multistage stress caused by the horizontal tectonic compression, burial depth, uplift, and denudation of heterogeneous rock formations. Zeng et al. (2007) also point out that the horizontal tectonic compression stress is the main source of force for the formation of fractures. Ju et al. (2020) study the effectiveness of Chang 7 cracks and suggest that the cracks are consistent with the horizontal maximum stress direction, and natural cracks with larger dip angles will be the first to become effective cracks. The acoustic emission experiment shows the fractures of the Yanchang Formation in the Ordos Basin are mainly formed in three periods, namely, the Indosinian, Yanshanian, and Himalayan periods (Guo et al., 2019; Shao et al., 2021). Zhang et al. (2021) simulate the stress field of Chang 7 in the Ansai area, and the results show there are more cracks in the high-stress area. Some methods

[1]China University of Petroleum, College of Geosciences, Beijing, China and China University of Petroleum, State Key Laboratory of Petroleum Resources and Prospecting, Beijing, China. E-mail: 3205275149@qq.com; liucl@cup.edu.cn (corresponding author); 1448906535@qq.com; rsageoche@gmail.com; 869221614@qq.com; 309167164@qq.com; 1666347539@qq.com; 1525907957@qq.com.

Manuscript received by the Editor 13 September 2021; revised manuscript received 16 January 2022; published ahead of production 17 March 2022; published online 18 May 2022. This paper appears in *Interpretation*, Vol. 10, No. 3 (August 2022); p. SJ15–SJ28, 16 FIGS., 6 TABLES.
http://dx.doi.org/10.1190/INT-2021-0181.1.

DOI:10.1190/INT-2021-0181.1

and technologies have been used to study and predict fractures in recent years, such as statistical methods based on core observations, curvature methods, and seismic methods. However, core observation can only identify a limited range of fractures in the well, and it is difficult to predict fractures in the well-free zone. Identifying fractures with conventional logging is difficult, whereas using image logging is more effective but costly, and the data are generally less. The accuracy of seismic fracture prediction is not high (Bahorich and Farmer, 1995; Pedersen and Skov, 2002). The tectonic curvature method often is used to predict the distribution of tensile fractures in the bending strata, but it cannot reflect the shear fractures. Moreover, this method is more suitable in regions with strong tectonic deformation. However, it does not have any obvious effect in the Ordos Basin with weak tectonic deformation (Guo et al., 1998; Ren et al., 2020). It is difficult to accurately evaluate the distribution of fractures outside the fault using the fractal dimension method because the fractures are completely subject to the development of the fault (Dai et al., 2011). The numerical simulation is a relatively reliable method for predicting tectonic fractures. Although the process of stress field simulation is complex, the boundary conditions need to be determined repeatedly. Therefore, this method can fully consider the fracture type, structure, fault, lithology, and other factors and achieve quantitative fracture prediction (Ding et al., 1998; Zeng and Xiao, 1999; Wu et al., 2018; Guo et al., 2019; Liu et al., 2019). In this study, the distribution of fractures is predicted by combining the rock failure criterion and stress field identified through stress numerical simulation, which provides an important basis for oil and gas exploration and exploitation.

Geologic setting

Ansai area is located in the central part of the Yishan Slope in the Ordos Basin (Figure 1). It has a simple monoclinal structure dipping to the west, and the dip angle is 0.5°C (Wang and Zhang, 2018). The Triassic Yanchang Formation in the Ordos Basin has developed fluvial-lacustrine-delta sedimentary facies (Yang et al., 2007). It is divided into 10 oil-bearing layers, and Chang 7 is the target oil-bearing layer of this study (Zhang et al., 2021). Ansai area mainly has developed shore-shallow lacustrine deposits as the result of standing away from the center of the lake basin and mainly deposited shale interbedded with tight sandstone (Yang et al., 2019). In the study area, natural fractures based on their genesis can be divided into tectonic fractures and nontectonic fractures. Tectonic fractures, such as tensile fractures and shear fractures, are formed by tectonic stress, whereas nontectonic fractures include fractures produced by diagenesis and bedding fractures. The objective of the numerical simulation results is to determine the tectonic fracture. Since Mesozoic, the Ordos Basin has experienced three tectonic movements: Indosinian orogeny, Yanshan orogeny, and Himalayan orogeny; the tectonic fractures are mainly formed during Yanshan orogeny and Himalayan orogeny. The tectonic fractures that developed during the Yanshan period are the east–west direction and northwest–southeast direction, whereas the tectonic fractures that developed during the Himalayan period are the north–south direction and northeast–southwest direction (Figure 2d) (Zeng and Zhao, 2019).

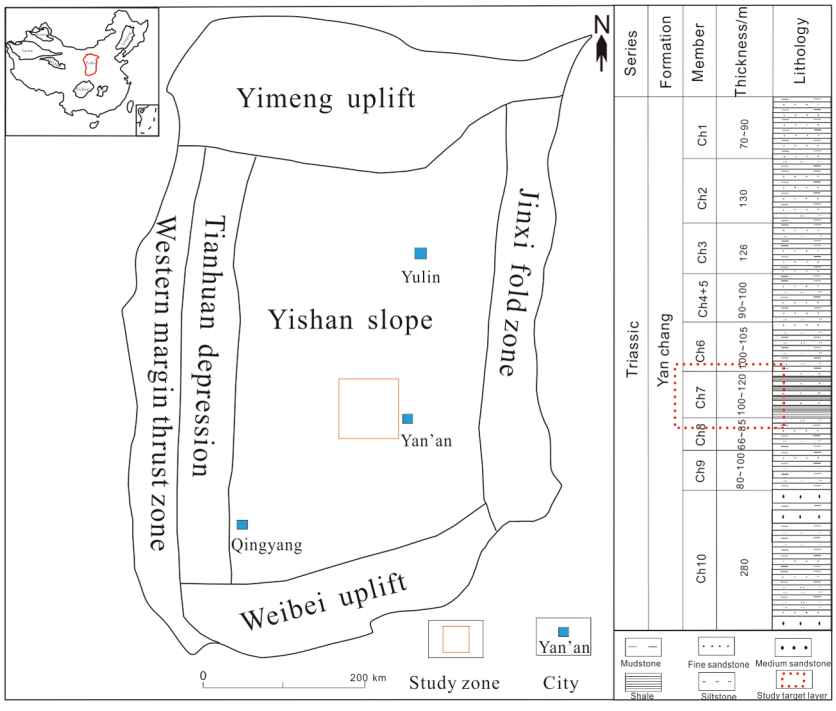

Figure 1. Location map and stratigraphic histogram of Chang 7 in the Ordos Basin (modified from Xu et al., 2022).

The characteristics of fractures

Fractures can be divided into macrofractures and microfractures based on their scale. The features of microfractures can be most effectively identified by analyzing the cores and outcrops sample. Moreover, image logging technology can be used to identify fractures and determine their strike and dip. Microfractures can be studied by casting thin sections and scanning by electron microscope. The fractures of Chang 7 in the Ansai area can be divided into nonstructural fractures and structural fractures based on their origin. Moreover, it includes shear fractures and tension fractures, in terms of mechanical properties. The surface of tension fractures is usually rough and uneven — small in scale — and does not largely extend (Figure 3a and 3b). Conversely, shear fractures are smooth and straight — largely extended — often cutting gravel (Figure 3c, 3d, and 3e). Diagenetic fractures refer to natural

fractures produced by diageneses, such as compaction and pressure solution. Horizontal bedding fractures are the most common diagenetic fracture in the study area usually forming along the bedding plane (Figure 3f). Microfractures refer to natural fractures that cannot be identified by the naked eye and require a microscopic identification to describe natural cracks. According to the relationship between fractures and mineral particles, microcracks can be classified into three types: cut-grain cracks, intragrain cracks, and grain-edge cracks. The characteristics of cut-grain cracks are as follows: these cracks are not restricted by mineral grains and can continuously cut through multiple mineral grains to extend (Figure 3g). Intragrain cracks are formed by the interaction of mutual squeezing between mineral particles, and they generally terminate at the edges of the particles (Figure 3h and 3i). Grain-edge cracks refer to the cracks distributed on the edges of mineral particles, which are related to the compaction and pressure solution during reservoir diagenesis (Figure 3j and 3k). The fracture length in Chang 7 reservoir from the Ansai area varies from 8 cm to 160 cm. Figure 2 illustrates that the fractures with a length of 10–40 cm are widely distributed, accounting for 45%. The second most identified fractures range from 40 cm to 80 cm, constituting 21%. The number of fractures larger than 80 cm and lower than 10 cm is the smallest, accounting for 16% and 18%, respectively. Fracture effectiveness is significant for understanding reservoir migration and water injection development. The research on the effectiveness of fractures mainly studies the minerals filled in the cracks and the degree of filling.

The fractures in the Chang 7 reservoir are mainly filled with calcite (Figure 3b and 3c), illite (Figure 3l), and asphalt (Figure 3a), which will reduce the effectiveness of the fractures. Figure 2b shows that the unfilled, partially filled, and fully filled fractures represent 46%, 42%, and 12%, respectively.

Imaging logging can intuitively and accurately determine fracture orientation. Due to the intrusion of mud into the unfilled cracks, the resistivity of the cracks is significantly lower than the surrounding rock. Therefore, the cracks appear as dark stripes on the imaging map

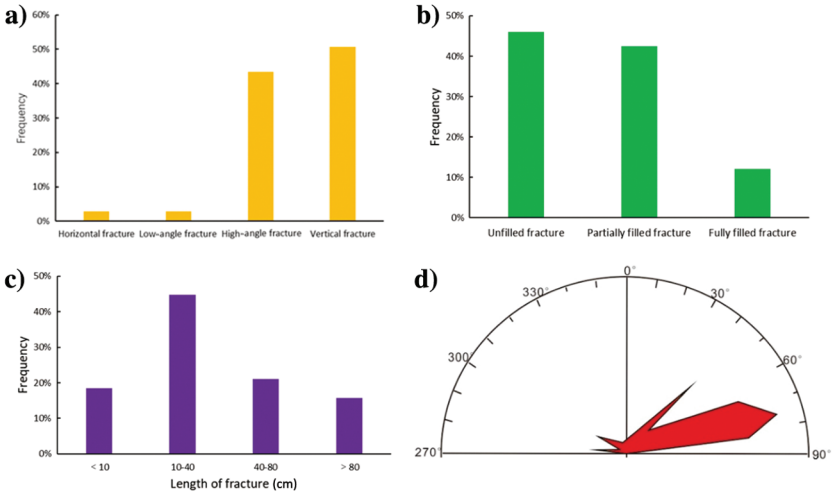

Figure 2. Fracture characteristic parameters of Chang 7 in Ansai area.

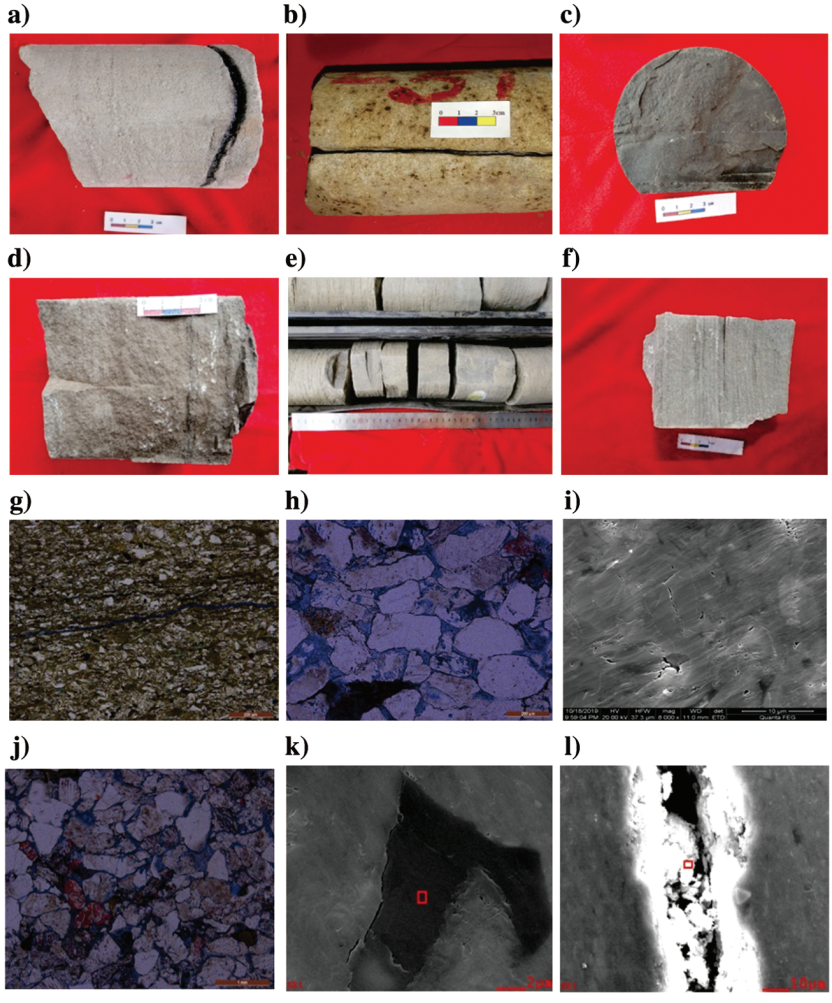

Figure 3. Fracture characteristics at different scales: (a) Q203 well, 1452.55 m, horizontal cracks filled with organic matter; (b) D126 well, 1913.83 m, a tension crack; (c) Q129 well, 1640.29 m, vertical shear cracks filled with calcite; (d) D76 well, 1627.36 m, high-angle shear fracture; (e) W533 well, 1530.06–1530.434 m, the surface of a high-angle crack; (f) D165 well, 1661.63 m, horizontal bedding cracks filled with asphalt; (g) Q71 well, 1422.22 m, cut-grain cracks; (h) Z22-31 well, 1248.26 m, intragrain cracks; (i) Q129 well, 1671.95 m, cracks inside the feldspar; (j) Z22-31 well, 1248.26 m, grain-edge cracks; (k) Q129 well,1667.48 m, grain-edge cracks; and (l) Q71 well, 1429.49 m, a crack filled with illite.

DOI:10.1190/INT-2021-0181.1

(Figure 4). However, some cracks are partially or fully filled by high-resistivity minerals, and those cracks appear as a bright sinusoidal curve (Figure 4). Fractures in Chang 7 can be divided into four types based on the size of the dip angle: horizontal fractures (0°–15°), low-angle fractures (15°–45°), high-angle fractures (45°–75°), and vertical fractures (75°–90°), accounting for 3%, 3%, 43%, and 51%, respectively (Figure 2a).

Determination of simulation parameters

The Ordos Basin has experienced three tectonic movements, i.e., the Indosinian movement, the Yanshan movement, and the Himalayan movement. In the Indonesian movement, the direction of tectonic stress with compressive trait was north–south. The Yanshanian movement showed the northwest-west and southeast compression, which led to northwest–southeast and east–west tectonic fractures. The Himalayan period is a key period that showed north-northeast–south-southwest compression (Wan, 1996; Zhang, 1996). Acoustic emission experiments can be used to determine the period and magnitude of tectonic stress (Zhao et al., 2022). Following the principle of the rock acoustic emission experiment, the external stress will break and produce an instantaneous elastic wave that is a phenomenon of acoustic release. Rocks have stress memory under the action of paleo-tectonic stress. Therefore, the rock will produce an obvious acoustic emission signal when the stress reaches or exceeds the paleo-stress (Lockner, 1993). This phenomenon is called the Kaiser effect (Liu et al., 2018a). Figure 5 shows that the Yanchang Formation in the Ordos Basin has three Kaiser effect points, reflecting that the study area has experienced three tectonic movement events. These three movements are the Indosinian movement, the Yanshan movement, and the Himalayan movement (Shao et al., 2021). Table 1 illustrates the stress in the Himalayan period is between 34.69 Mpa and 49.18 MPa. Triaxial stress test of rock illustrates that the deformation has been mostly elastic before rock failure, and burst exhibited an evident decrease in stress after fracturing (Figure 6). Thus, the elastic model has been used to simulate the geologic body (Wang et al., 2004). According to the resolution and stress composition, the stress from south to north is 12 MPa, whereas the stress from west to east is 29 MPa. The overburden pressure within the model has been calculated via the density of the rock layers and acceleration, and the magnitude is 50 MPa. Therefore, the following boundary conditions for the geologic model have been established in the tectonic stress field simulation of the Himalayan period: the model's constrained area is located at the bottom of the model, as well as the northern and eastern model boundaries. The western boundary of the model is loaded with a stress of 29 MPa, whereas the southern boundary is loaded with a stress of 12 MPa. Moreover, the downward concentration perpendicular to the model (stratum) is 50 MPa (Figure 7).

Mechanical parameters, such as Young's modulus and Poisson's ratio, are essential in reflecting rock properties. Young's modulus and Poisson's ratio can be classified into dynamic and static. The dynamic parameters that are easier to acquire than static parameters can be determined by logging data and formulas 4 and 5. The transverse wave offset time is obtained by formula 3. It can be obtained by mathematical fitting of the transverse wave offset time and the longitudinal wave offset time measured by logging (Table 2). The static parameters identified by the stress test in a laboratory are more accurate than the dynamic parameters, which is relatively more expensive.

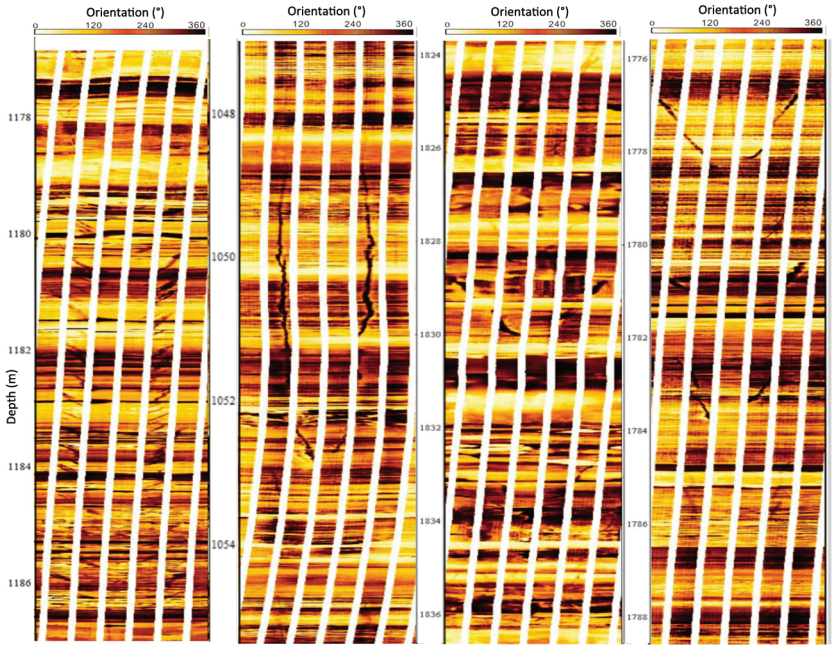

Figure 4. Identification of fractures by imaging logging.

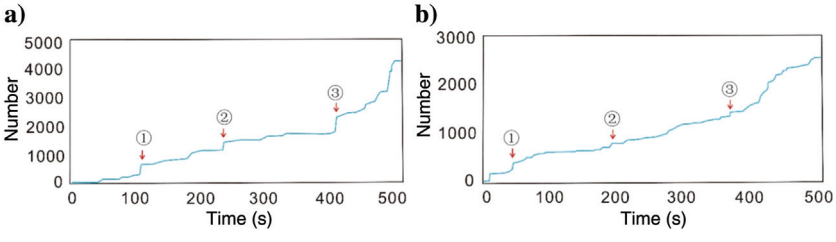

Figure 5. Curve of rock acoustic emission (from Shao et al., 2021): (a) Y177 well, Yanchang Formation, 2192 m and (b) F34 well, Yanchang Formation, 2417 m.

DOI:10.1190/INT-2021-0181.1

DOI:10.1190/INT-2021-0181.1

The mechanical parameters of the rock can be determined by a uniaxial stress test or triaxial stress test in the laboratory (Tani et al., 2003). In uniaxial stress tests, pressure is applied along the core sample axis and slowly increases the pressure until the rock ruptures. The key point of the uniaxial stress test is to slowly increase the pressure on the core sample until the rock fractures under the condition of applying an axial pressure without confining pressure. The parameters that the uniaxial stress test can measure are compressive strength, Poisson's ratio, Young's modulus, shear modulus, and bulk modulus. However, in the triaxial stress test, the axial pressure and the confining pressure are applied to the rock sample. The triaxial stress test can determine compressive strength, Poisson's ratio, Young's modulus, shear modulus, bulk modulus, internal friction angle, cohesion, etc. (Mousavi et al., 2019). The rocks undergo an anisotropic stress field. In other words, the rock in the actual formation is subjected to triaxial stress. Compared with the uniaxial stress test, the triaxial stress test can measure more parameters, and the force state of the rock is consistent with the rock underground. Therefore, in this study, the mechanical parameters of the rock are determined by a triaxial stress test. The RETS-2000/120 rock mechanics triaxial test system is used for this research. A maximum vertical load of 2.000.0 kN is applied to a rock sample whose size is Φ 25.4 mm $\times$ h 50 mm, and the loading rate is 200 kN/min. The confining pressure gradually increases, and the rate of loading is between 0.001 MPa/s and 1.0 MPa/s. First, the sample is wrapped with a heat-shrinkable tube and placed in the high-pressure chamber, and then the strain measuring device and heating accessories are connected to the system. The next step is to fill the chamber with confining pressure liquid and set the confining pressure that should be continuously loaded to the desired value within 5 min. The axial load can be applied after the confining pressure is stable. The temperature ranges from 23°C to 25°C. The triaxial stress test can generate the relationship curve between the stress and strain of the rock sample, which shows that, as the strain increases, the stress increases. However, when the rock breaks, the stress decreases instantly. Moreover, the mechanical parameters of the rock can be calculated according to the relationship between stress and strain.

The rock's compressive strength is the rock's ultimate strength when it ruptures under uniaxial pressure, which is equal to the maximum axial stress when the rock ruptures (Mokhtarian et al., 2020). It is worth mentioning that the stress at the inflection point of the stress-strain curve represents the compressive strength (Figure 6). Figure 6 and Table 3 illustrate that the compressive strength of rock varies from 10.43 MPa to 151.79 MPa. The main reason for this is attributed to the horizontal bedding. Specifically, the sample's compressive strength with the axial load applied along the horizontal bedding is relatively low. In contrast, the sample's compressive strength with the axial load applied perpendicularly to the horizontal bedding and the sample with a block structure is relatively high. In addition, Figure 6 shows that the fractures in the experiment are mostly vertical and high-angle cracks, which is consistent with fractures on the core.

Young's modulus is the ratio of stress to strain in the elastic range of the rock:

$$E = \frac{\Delta\sigma}{\Delta\varepsilon_a}, \tag{1}$$

where E is the Young's modulus, that is, the slope of the stress-strain curve, and $\Delta\sigma$ and $\Delta\varepsilon_a$ are the increments of axial stress and axial strain, respectively.

Poisson's ratio is the ratio of the radial strain to the axial strain of the rock under compression:

$$\mu = -\frac{\varepsilon_c}{\varepsilon_a}, \tag{2}$$

where μ is the Poisson's ratio and ε_c and ε_a are the radial strain and axial strain, respectively.

Figure 8a and 8b shows that the major portion of static Poisson's ratio ranges from 0.18 to 0.265, lower than the dynamic Poisson's ratio ranging from 0.322 to 0.333. Figure 8c shows the static Young's modulus ranges from 9.43 GPa to 40.64 GPa. It has a characteristic of uniform distribution, which is similar to dynamic Young's modulus ranging from 15.01 GPa to 39 GPa (Figure 8d). In addition, Figure 8d shows that Young's modulus of shale is less than Young's modulus of sandstone. In contrast, Poisson's ratio of shale is higher than Poisson's ratio of sandstone.

According to the preceding description, there is a certain transformation relationship between static parameters and dynamic parameters. The dynamic parameters can be corrected through static parameters by using the linear fit to make the dynamic parameters more reliable (Figure 9a and 9b). Figure 9c indicates the source of compressive strength that is an indispensable

Table 1. The result of tectonic stress measurement from the acoustic emissions (from Guo et al., 2019).

Samples	Stress (MPa)	Main tectonic movement
E33	34.69	Himalayan
S389-1	41.22	
L17	42.86	
S389-2	44.9	
S310	49.18	
S337	61.22	Yanshanian
S318	65.3	
S410	68.57	
S256	69.8	
L6	85.7	Indosinian
S307	86.73	
S280-1	102.04	
S280-2	102.04	

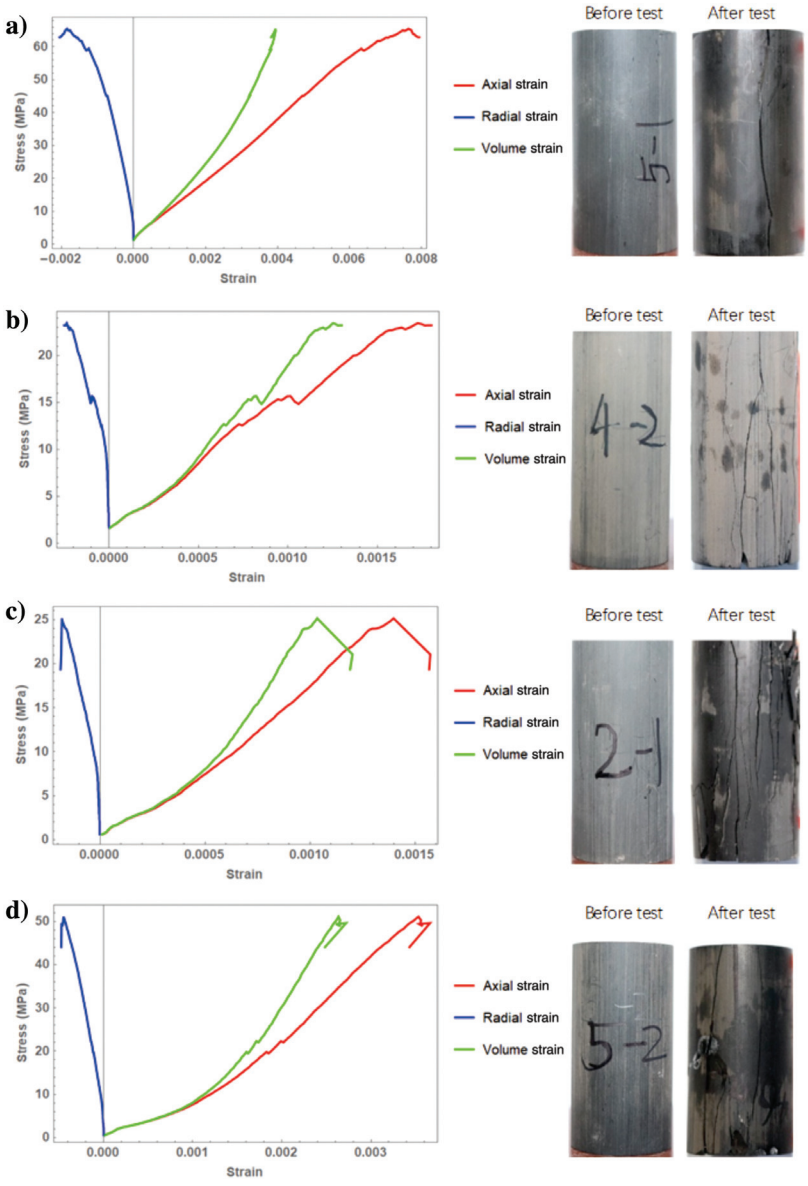

Figure 6. Graph of triaxial stress experiment: (a) sample 5-1, Q129 well, −1646.75 m, Chang 7, shale; (b) sample 4-2, Q71 well, −1429.51 m, Chang 7, shale; (c) sample 2-1, Q71 well, −1426.25 m, Chang 7, shale; and (d) sample 5-2, Q129 well, −1646.72 m, Chang 7, shale.

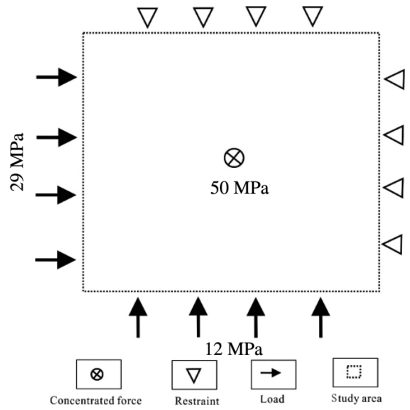

Figure 7. Boundary conditions.

parameter in simulation. In this study, the linear fitting formulas are presented in equations 6 and 7:

$$\Delta t_s = \frac{\Delta t_p}{\left[1 - 1.15\frac{\left(\frac{1}{\rho_b}\right)+\left(\frac{1}{\rho_b}\right)^3}{e^{1/\rho_b}}\right]^{1.5}}, \quad (3)$$

$$\mu_d = \frac{\Delta t_s^2 - 2\Delta t_p^2}{2(\Delta t_s^2 - \Delta t_p^2)}, \quad (4)$$

$$Ed = \frac{\rho_b(3\Delta t_s^2 - 4\Delta t_p^2)}{\Delta t_s^2(\Delta t_s^2 - \Delta t_p^2)} \times 9.29 \times 10^7, \quad (5)$$

$$\mu = 0.3471\mu_d + 0.1091, \quad (6)$$

$$E = 0.5334Ed + 8407.2, \quad (7)$$

where μ_d is the dynamic Poisson's ratio (dimensionless), Ed is the dynamic Young's modulus in GPa, μ is the corrected Poisson's ratio (dimensionless), E is the corrected Young's modulus in GPa, Δt_s is the transverse wave offset time in μs/m, Δt_p is the longitudinal wave offset time in μs/m, and ρ_b is the rock density in g/cm^3.

Table 4 shows the static Poisson's ratio ranges from 0.190 to 0.254, and the corrected Poisson's ratio ranges from 0.224 to 0.240. The relative error of Poisson's ratio ranges from 24.74% to 2.44%. The static Young's modulus ranges from 14.94 GPa to 39.30 GPa, and the corrected Young's modulus ranges from 16.96 GPa to 37.99 GPa. The relative error of Young's modulus ranges from 36.42% to 3.34%. Both parameters have a credible correction.

Figure 10 shows the mechanical parameters of three sublayers, including Chang 7_1, Chang 7_2, and Chang 7_3. Chang 7_1 has Young's modulus ranging from 16 GPa to 40 GPa, with high-value areas primarily located in the southwest and northeast. The Young's modulus of Chang 7_2 varies between 17 GPa and 42 GPa, with the low-value area located in the southwest. The Young's modulus of Chang 7_3 varies between 15 GPa and 40 GPa, with the highest value area located in the west. The Poisson's ratio of three sublayers runs from 0.215 to 0.239, and it displays a band-like distribution.

Establishment of simulation models

The purpose of establishing a model is to make the stress state of the geologic body more consistent with the actual geologic situation. The key point of simulation is to deal with the key parameters affecting the stress field in detail. The process of establishing models includes establishing a geologic model, building a mechanical model, and identifying boundary conditions (Figure 7) by applying force, load, and restraint on geologic models (Liu et al., 2018a). It is undeniable that the consistency of the geologic model is crucial because it is one of the important factors affecting the accuracy of simulation results. The simulation results will be more accurate if the model is more comparable with the geologic body. In this study, the geologic model is established by using SUFER and ANSYS (Figure 11), and 527,684 nodes are set, which meets the basic requirements. The planar anisotropy of the mechanical parameters is stronger than the anisotropy among sublayers, as shown in Figure 10. Therefore, the mechanical parameters put on the model are divided into four portions (Table 5) based on the plane distribution characteristics to rationalize and simplify the simulation process. The thickness change of the Chang 7 oil-bearing layer is small, mainly between 93 m and 99 m. Therefore, the loaded stratum thickness value is set to be 96 m (Figure 12).

Table 2. Data of transverse and longitudinal wave offset time from logging.

Longitudinal wave offset time (μs/m)	Rock density (g/cm^3)	Transverse wave offset time (μs/m)
307.23	2.43	609.04
303.65	2.47	594.95
315.34	2.41	630.29
307.13	2.45	604.90
222.73	2.54	427.61
227.07	2.60	428.62
287.07	2.47	562.31
309.04	2.41	617.70
224.68	2.58	426.50
303.65	2.47	594.95
301.68	2.47	590.92
299.88	2.46	589.53

Results of stress field simulation

The maximum principal stress value distribution ranges from 32 MPa to 28 MPa (Figure 13a). The areas with the maximum principal stress greater than 30.2 MPa are chiefly distributed in the eastern parts of the Ansai

Table 3. Results of triaxial stress test.

Sample number	Depth (m)	Direction of sample	Lithology	Diameter (mm)	Height (mm)	Confining pressure (MPa)	Compressive strength (MPa)	Young's modulus (GPa)	Poisson's ratio
1-1	1435.50	Vertical	Argillaceous sandstone	25.26	55.00	0	110.78	39.30	0.210
3-2	1429.62	Horizontal	Shale	25.40	49.60	0	24.49	23.09	0.250
7-1	1418.88	Horizontal	Argillaceous sandstone	25.09	40.55	0	50.74	31.38	0.235
8-1	1427.25	Vertical	Shale	25.40	33.99	0	35.71	19.19	0.254
6-2	1431.50	Horizontal	Shale	25.25	37.95	0	10.43	9.43	0.263
4-2	1429.75	Horizontal	Shale	25.40	39.30	0	32.73	25.78	0.232
2-1	1426.25	Horizontal	Shale	25.39	36.85	0	15.10	14.94	0.246
1-2	1434.63	Vertical	Argillaceous sandstone	25.10	54.63	15	80.43	22.08	0.210
7-2	1418.25	Horizontal	Argillaceous sandstone	25.32	47.10	15	78.35	17.10	0.220
2-1	1426.50	Horizontal	Shale	25.38	56.14	0	25.15	21.31	0.190
4-2	1429.63	Horizontal	Shale	25.65	63.12	0	23.47	12.78	0.190
2-2	1426.63	Horizontal	Shale	25.23	50.24	15	111.68	40.64	0.350
4-1	1429.51	Horizontal	Shale	25.69	49.96	15	116.07	36.06	0.230
9-1	1436.38	Vertical	Argillaceous sandstone	25.01	41.31	15	151.79	25.65	0.230
8-4	1427.50	Vertical	Shale	25.50	31.06	14	65.48	10.29	0.220
8-3	1427.38	Vertical	Shale	25.40	49.96	17	124.07	15.40	0.210
5-2	1646.72	Horizontal	Shale	25.19	49.62	0	51.07	20.62	0.180
5-1	1646.75	Horizontal	Shale	25.38	50.02	15	106.75	32.08	0.220
5-3	1646.80	Horizontal	Shale	25.40	39.51	0	15.83	11.09	0.185

DOI:10.1190/INT-2021-0181.1

area. In contrast, the areas with the maximum principal stress lower than 29 MPa are mainly distributed in the southeast part. Overall, the maximum principal stress gradually decreases from east to west. It can reflect the degree of tectonic deformation to some extent when the minimum principal stress is small. There is significant differentiation in minimum principal stress between east and west (Figure 13b). The minimum principal stress of greater than 9.8 MPa is in the southeast corner, whereas the lower than 9.2 MPa is encountered in the western parts of the area. Figure 13c illustrates the value of differential stress ranges from 17 MPa to 25 MPa. In the study area, the maximum differential stress greater than 20.5 MPa is noticed in the central-eastern and western parts. The northern and southeastern parts have minimum differential stress of less than 19 MPa. The comparison of Figures 11 and 13c shows that the areas with high differential stress correspond with areas of raised topography. It indicates the differential stress can reflect the degree of tectonic deformation. In other words, the greater the differential stress, the stronger the tectonic effect.

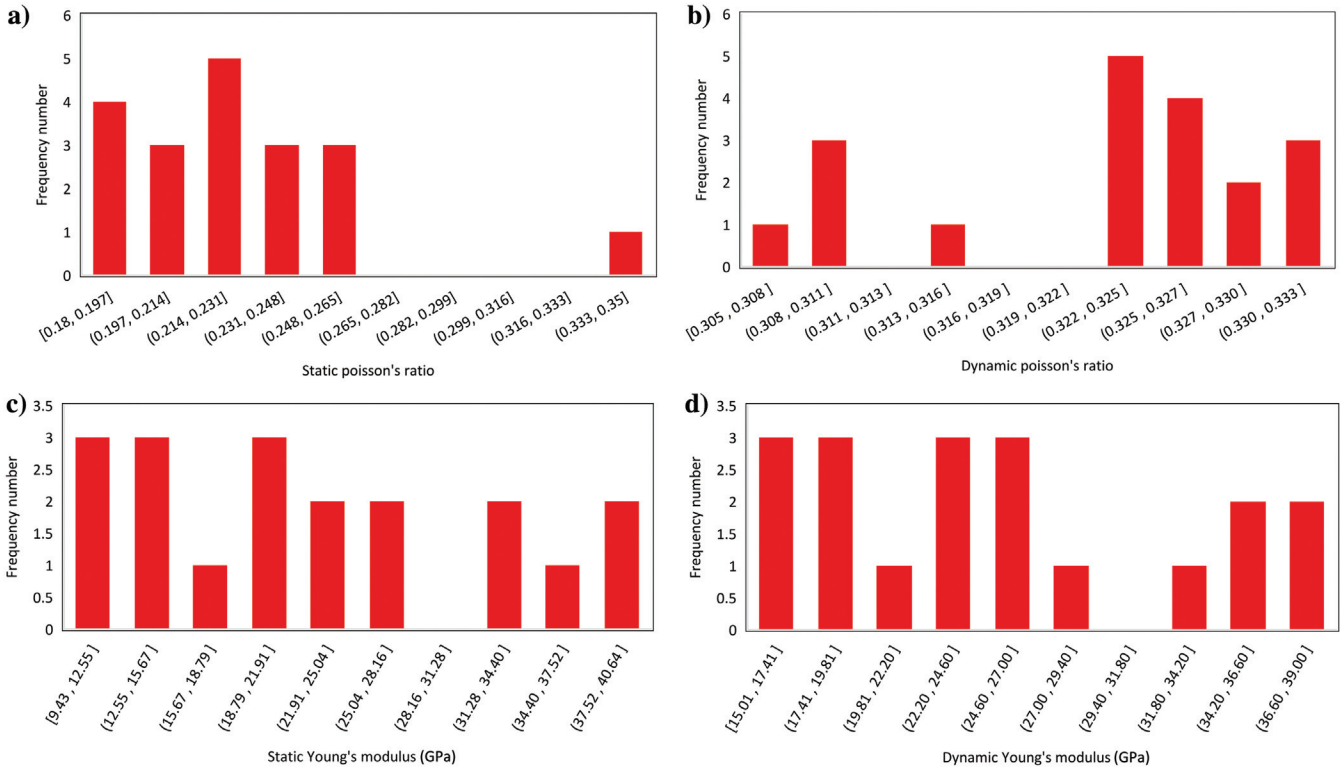

Figure 8. (a) Frequency histogram of static Poisson's ratio, (b) frequency histogram of dynamic Poisson's ratio, (c) frequency histogram of static Young's modulus, and (d) frequency histogram of dynamic Young's modulus.

Figure 9. Fitting curve (a) between static and dynamic Poisson's ratio, (b) between static and dynamic Young's modulus, and (c) between Young's modulus and compressive strength, and (d) relationship between lithology and mechanical parameters.

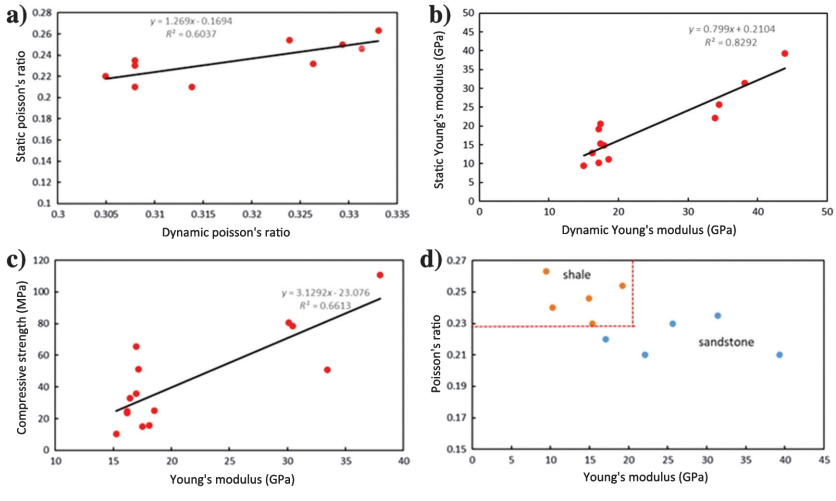

DOI:10.1190/INT-2021-0181.1

Fracture prediction

Griffith criterion

The Griffith criterion can judge the tensile fracture of elastic rock mass with brittle properties. According to Griffith's criterion, the generation of fractures is due to randomly distributed microcracks in the rock. Moreover, when the rock is subjected to external forces, the edges of these microcracks will extend to form macroscopic fractures. The rupture criterion is as follows:

Table 4. Error analysis of mechanical parameters.

Static Poisson's ratio	Corrected Poisson's ratio	Relative error (%)	Static Young's modulus (GPa)	Corrected Young's modulus (GPa)	Relative error (%)
0.210	0.224	6.67	39.30	37.99	3.34
0.250	0.239	4.40	23.09	16.19	29.87
0.235	0.224	4.68	31.38	33.42	6.49
0.254	0.235	7.48	19.19	16.96	11.64
0.246	0.240	2.44	14.94	17.53	17.33
0.210	0.228	8.57	22.08	30.12	36.42
0.190	0.237	24.74	21.31	18.54	13.01
0.230	0.224	2.61	25.65	30.57	19.18
0.210	0.235	11.90	15.40	17.14	11.33

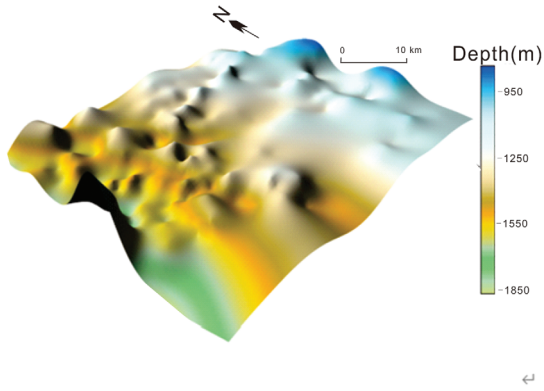

Figure 11. Structure of Chang 7 in Ansai area.

Table 5. Mechanical parameters assignment table.

Zone	Young's modulus (GPa)	Poisson's ratio
A	28	0.230
B	30	0.220
C	32	0.225
D	28	0.240

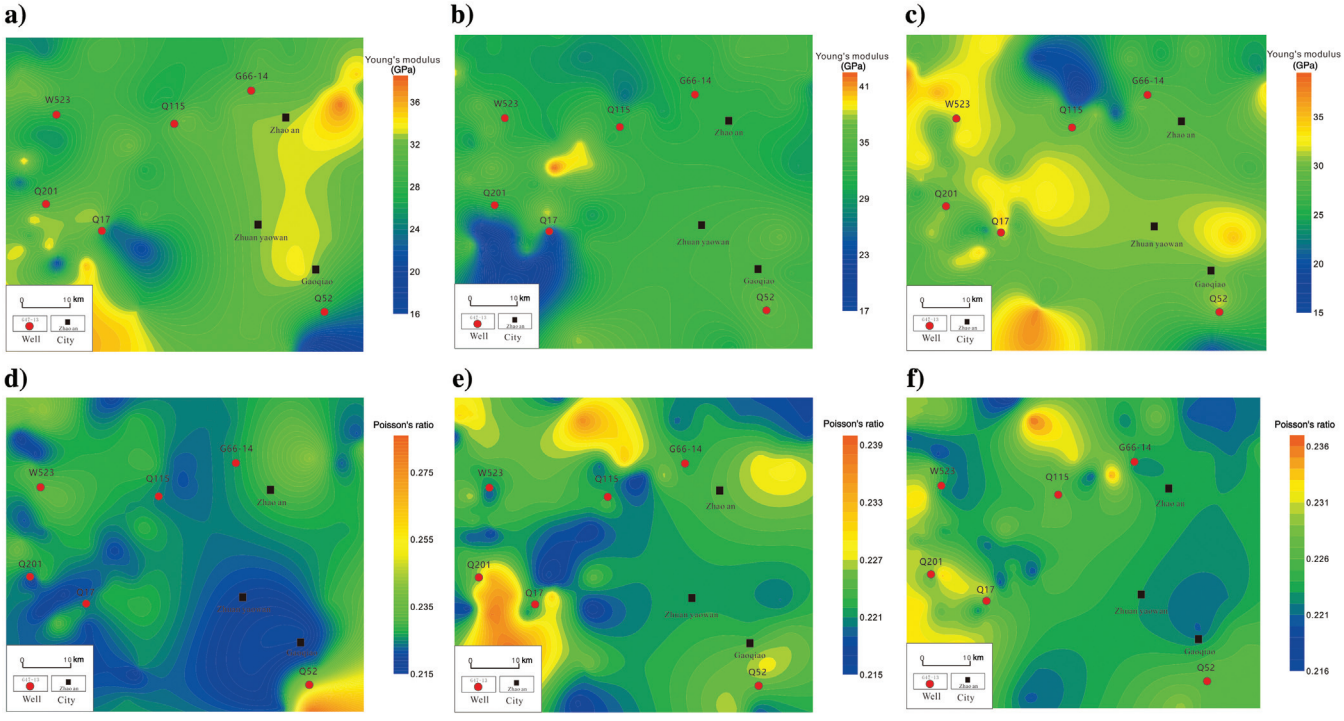

Figure 10. Distribution of mechanical parameters: (a) Young's modulus in Chang 7_1 of Ansai, (b) Young's modulus in Chang 7_2 of Ansai, (c) Young's modulus in Chang 7_3 of Ansai, (d) Poisson's ratio in Chang 7_1 of Ansai, (e) Poisson's ratio in Chang 7_2 of Ansai, and (f) Poisson's ratio in Chang 7_3 of Ansai.

For $\sigma_2 + 3\sigma_1 \geq 0$:

$$(\sigma_1 - \sigma_2)^2 + 8(\sigma_1 + \sigma_2)\sigma_T = 0; \tag{8}$$

For $\sigma_2 + 3\sigma_1 < 0$:

$$-\sigma_2 = \sigma_T, \tag{9}$$

where σ_1 is the maximum principal stress, σ_2 is the minimum principal stress, and σ_T is the effective tensile stress.

The tensile strength describes the degree of tension. In other words, the larger the value, the greater the degree of tensile and the more developed the tensile fracture. The rate of tensile fracture can be determined to describe the degree of tensile fracture quantitatively. The following formula can determine it:

$$I_1 = \sigma_T/|\sigma_T|, \tag{10}$$

where $|\sigma_T|$ is the tensile strength and I_1 is the tensile fracture rate. It is indicated the tensile fracture developed when the I_1 is more than 1. Moreover, the higher the value, the greater the tensile fractures.

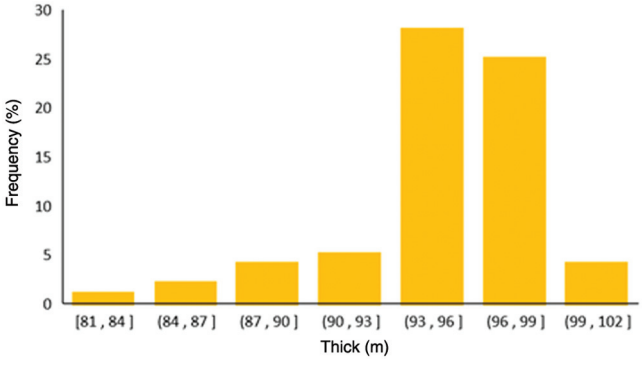

Figure 12. Histogram of stratum thickness.

Mohr-Coulomb criterion

The Mohr-Coulomb criterion indicates that the rock fracture occurs when the rock is subjected to stress and the weaker structural planes in rock are subjected to shear stress. The cause of shear fracture is the shear stress and normal stress on the weaker structural plane. It can be determined as

$$|\tau| = C + \sigma_n \tan \varphi, \tag{11}$$

$$\tau_n = \frac{\sigma_1 - \sigma_2}{2} \sin 2\alpha, \tag{12}$$

$$\sigma_n = \frac{\sigma_1 + \sigma_2}{2} + \frac{\sigma_1 - \sigma_2}{2} \cos 2\alpha, \tag{13}$$

$$\sin 2\alpha = \frac{1}{\sqrt{1 + \mu^2}}, \tag{14}$$

$$\cos 2\alpha = \frac{-\mu}{\sqrt{1 + \mu^2}}, \tag{15}$$

where σ_n is the normal stress, τ_n is the shear stress, $|\tau|$ is the shear strength, C is the cohesion, and φ is the angle of internal friction.

Similarly, the shear failure rate is introduced to describe the development of shear fractures quantitatively. The following formula can calculate the shear failure rate:

$$I_2 = \tau_n/|\tau|, \tag{16}$$

where I_2 is the shear failure rate. It is suggested that when I_2 increased more than 1.0, the shear fracture develops. However, the larger the I_2, the more the shear fractures.

The tensile fractures in the study area mainly range from 1.05 to 0.97 (Figure 14a). The higher tensile

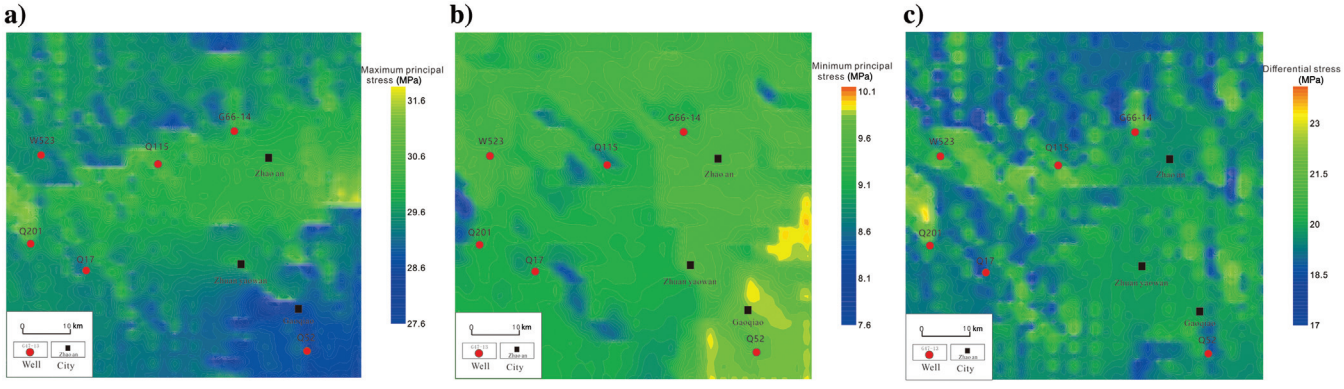

Figure 13. Plane distribution of stress in Ansai: (a) the maximum principal stress in Chang 7, (b) the minimum principal stress in Chang 7, and (c) the differential stress in Chang 7.

DOI:10.1190/INT-2021-0181.1

fractures are identified in the southeastern part of the study area, revealing a favorable region for the development of tensile fractures. Similarly, the shear fractures in the research area range from 1.02 and 0.98 (Figure 14b). It has a gradually decreasing trend from east to west, which reflects shear fractures that are more likely to develop in the eastern part.

Predicting fracture density by "two-factor method"

The two-factor method is a credible method predicting fracture density by combining comprehensive fracture rate and rock strain energy (Zhang et al., 2015). The comprehensive fracture rate is an indicator that reflects total fracture density, including the tension fractures and the shear fractures. It can be determined as follows:

$$I = aI_1 + bI_2, \tag{17}$$

where a and b represent the percentage of tension fractures with 20% (32 strips) and shear fractures with 80% (128 strips), respectively. It is obtained by observing the number of fractures on the core. Moreover, when I increases more than 1.0, the fractures are developed. Hence, the larger I is, the more fractures in the Ansai area. The comprehensive fracture rate cannot accurately reflect the degree of fracture development. It is due to the different sizes of two Moire circles with different rock strain energy. However, their comprehensive fracture rates are equal. Therefore, the rock strain energy also is related to the development of fractures. It can be calculated as follows:

$$W = [\sigma_1^2 + \sigma_2^2 + \sigma_3^2 - 2\mu(\sigma_1\sigma_2 + \sigma_1\sigma_3 + \sigma_2\sigma_3)]/2/E, \tag{18}$$

where σ_1, σ_2, and σ_3 are the three principal stresses, E is the Young's modulus, μ is the Poisson's ratio, and W is the rock strain energy.

The rock strain energy ranges from 0.0114 J to 0.0149 J (Figure 15). Its maximum value is identified in the mideastern part of the study area, whereas its minimum values are noticed in the southeastern region.

In this study, the comprehensive fracture density (A) is acquired by combining comprehensive fracture rate and rock strain energy. The constants in formula 19 can be acquired by analyzing cores through inversion using statistical fracture density. The fitting formula is as follows:

$$A = 430.87I^2 + 144381w^2 - 373.68I + 13520.11W - 9861.05WI + 283.79. \tag{19}$$

The fracture density of Chang 7 from the Ansai area ranges from 0 to 1.5 strips/m (Figure 16), whereas the fracture densities in most regions are between 0.2 strips/m and 0.4 strips/m. The fractures are mostly developed and distributed in the southeastern and some of the western parts. The fracture density has a banding plane distribution feature similar to mechanical parameters. It indicates that the anisotropy of mechanical parameters is the main reason for the distribution of fractures (Li et al., 2006; Zeng, 2008; Liu et al., 2018a). Comparing three stress figures with the distribution of fracture density, the stronger the tectonic stress, the more developed the fractures. It is suggested that the tectonic stress is an important external factor affecting the distribution of tectonic fractures. Table 6 shows the relative errors of fracture density range from 1.4% to 36.1%. The relative errors in seven wells are less than 30%, which indicates the applicability of formula 19 is good (Su et al., 2021). The error is mainly derived from the accuracy of the geologic model because it is impossible to get a very accurate paleo-structural map. Therefore, it is reasonable to

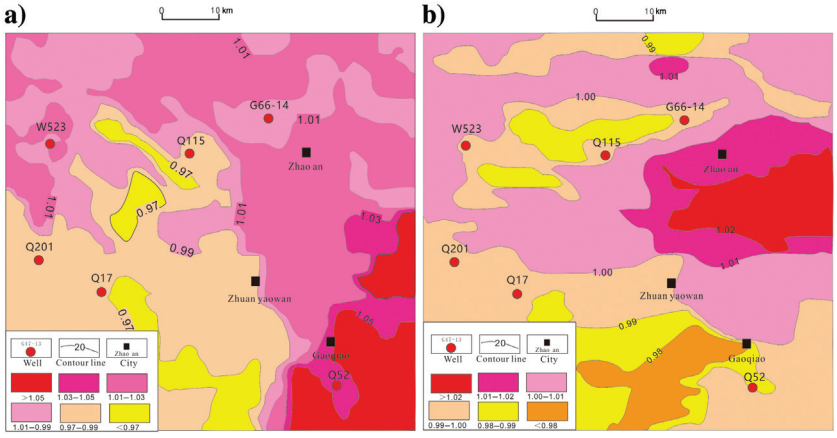

Figure 14. Plane distribution of fracture rate in Ansai area: (a) tensile fracture rate in Chang 7 and (b) shear fracture rate in Chang 7.

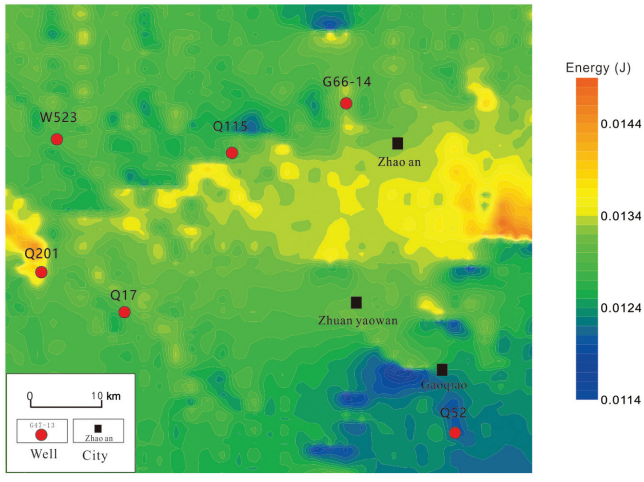

Figure 15. Plane distribution of rock strain energy in Chang 7 of Ansai area.

have simulated fracture or stress values errors. Moreover, there are numerous factors that influence the formation of cracks. The rock composition, granularity, and porosity can result in varying fracture abundances. In general, rocks with more quartz and feldspar are more likely to develop cracks, and low-porosity and fine-grained rocks are more likely to develop cracks. The reason is that the increase in the content of quartz and feldspar will increase the brittleness of the rock and make the rock more prone to cracks (Liu et al., 2018a). In contrast, shale with a significant amount of clay or organic content has creep deformation; hence, it has low fracture densities (Gu et al., 2020). The content of TOC also will influence the formation of cracks, but the relationship between the two is unclear. In other words, increasing the TOC content can either increase or decrease the density of cracks (Liu et al., 2018a; Zhao et al., 2020). Therefore, these factors influencing fracture development will be increased or decreased according to the characteristics of reservoirs with different properties when we apply the numerical simulation methods to predict fractures.

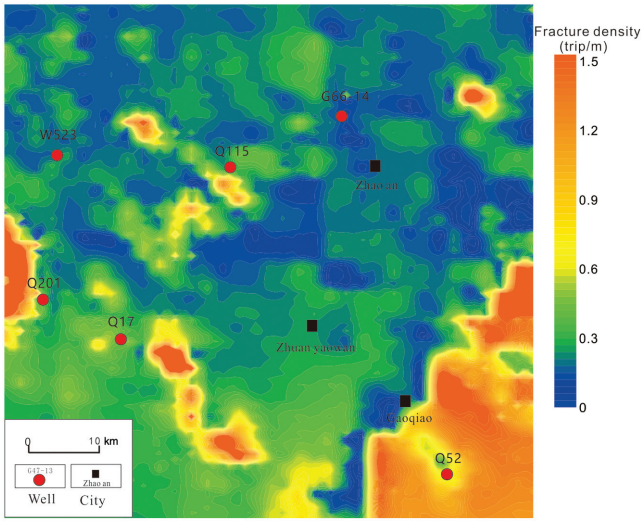

Figure 16. Plane distribution of fracture density in Chang 7 of Ansai area.

Table 6. Error analysis between core observation and prediction.

Well	Density of observation (strip/m)	Density of prediction (strip/m)	Relative error (%)
D199	0.04	0.05	19.61
W533	0.13	0.17	36.11
Q124	0.19	0.18	8.01
D113	0.22	0.21	4.67
Q99	0.33	0.37	11.30
Q113	0.30	0.22	27.79
D127	0.11	0.09	20.49
D228	0.10	0.11	1.49

Conclusion

This research has developed the simulation of tectonic stress and predicted the tectonic fractures in the Ansai area shale reservoirs from the Ordos Basin, China, using the scanning electron microscope, cores, thin sections, and image logging. Moreover, ANSYS is used to simulate the Himalayan stress field, whereas the two-factor method is used to predict the distribution of tectonic fracture by combining stress field and fracture criterion. The following are the outcomes of this research.

Chang 7 oil-bearing layer in the Ansai area mainly developed high-angle shear fractures in the northeast direction under the action of tectonic stress, and the effectiveness of the fractures is relatively high.

The compressive strength of the rock is related to the structure of the rock. Specifically, the more developed the horizontal bedding of the rock, the lower the compressive strength.

The value of mechanical parameters is related to lithology. This research shows that the Young's modulus of shale is lower than that of sandstone, whereas the Poisson's ratio of shale is higher than that of sandstone. Moreover, the degree of structural deformation is closely related to the differential stress, and the greater the differential stress, the stronger the structural deformation.

Stress and mechanical parameters are the two main factors affecting the development of structural fractures. Stress is an external factor that affects the development of tectonic fractures, whereas the mechanical parameters affect the anisotropy of fractures.

Acknowledgments

This research was supported by the National Natural Science Foundation of China (grant no. 41872127). The authors would like to thank all the staff of laboratories and people who collected the data about this research.

Data and materials availability

Data associated with this research are available and can be obtained by contacting the corresponding author.

References

Bahorich, M. S., and S. L. Farmer, 1995, 3-D seismic coherency for faults and stratigraphic features: The Leading Edge, **14**, 1053–1058, doi: 10.1190/1.1437077.

Cui, J. W., R. K. Zhu, C. Y. Fan, S. X. Li, Z. G. Mao, S. Li, and Z. Y. Zhang, 2019, Oil and gas resources of shale formation orderly accumulation and coexistence as well as its prospecting significance: A case study of Chang 7 shale formation in Ordos Basin: Geological Bulletin of China, **38**, 1052–1061.

Dai, J. S., Z. D. Feng, H. L. Liu, J. B. Zhang, and K. F. Jia, 2011, Analysis for the applicable conditions of several methods of reservoir fracture evaluation (in Chinese): Progress in Geophysics, **26**, 1234–1242.

Ding, Z. Y., X. L. Qian, H. Huo, and Y. Q. Yang, 1998, A new method for quantitative prediction of tectonic fractures — Two-factor method: Oil & Gas Geology, **19**, 1–14.

Gu, Y., W. L. Ding, Q. N. Tian, S. Xu, W. Zhang, B. R. Zhang, and B. C. Jiao, 2020, Developmental characteristics and dominant factors of natural fractures in lower Silurian marine organic-rich shale reservoirs: A case study of the Longmaxi Formation in the Fenggang block, southern China: Journal of Petroleum Science and Engineering, **192**, 107277, doi: 10.1016/j.petrol.2020.107277.

Guo, K., Z. Y. Xu, and G. S. Ni, 1998, Research on the main curvature method and its application to cracky oil-gas deposits: Computing Techniques for Geophysical and Geochemical Exploration, **20**, 335–337.

Guo, P., D. H. Ren, and Y. H. Xue, 2019, Simulation of multi-period tectonic stress fields and distribution prediction of tectonic fractures in tight gas reservoirs: A case study of the Tianhuan depression in western Ordos Basin, China: Marine and Petroleum Geology, **109**, 530–546, doi: 10.1016/j.marpetgeo.2019.06.026.

Ju, W., X. B. Niu, S. B. Feng, Y. You, H. R. Xu, and S. Y. Wang, 2020, The present-day in-situ stress state and fracture effectiveness evaluation in shale oil reservoir: A case study of the Yanchang Formation Chang7 oil-bearing layer in Ordos Basin: Journal of China University of Mining and Technology, **49**, 931–940.

Li, J., M. Chen, and G. H. Liu, 2006, Experimental orthotropic analysis of rock mechanics property: Journal of Southwest Petroleum Institute, **28**, 50.

Liu, C., X. Wang, C. H. Zhao, and S. Yin, 2019, Paleotectonic stress field simulation and fracture prediction of tight sandstone in the Shanxi Formation, southern Qinshui Basin, China: Geophysical Prospecting for Petroleum, **58**, 292–302.

Liu, J. S., W. L. Ding, H. M. Yang, K. Jiu, Z. Wang, and A. Li, 2018a, Quantitative prediction of fractures using the finite element method: A case study of the lower Silurian Longmaxi Formation in northern Guizhou, South China: Journal of Asian Earth Sciences, **154**, 397–418, doi: 10.1016/j.jseaes.2017.12.038.

Liu, Q., X. J. Yuan, S. H. Lin, H. Guo, and D. W. Cheng, 2018b, Depositional environment and characteristic comparison between lacustrine mudstone and shale: A case study from the Chang 7 member of the Yanchang Formation, Ordos Basin: Oil & Gas Geology, **39**, 531–540.

Lockner, D., 1993, The role of acoustic emission in the study of rock fracture: International Journal of Rock Mechanics and Mining Sciences & Geomechanics Abstracts, **30**, 883–899, doi: 10.1016/0148-9062(93)90041-B.

Mokhtarian, H., H. Moomivand, and H. Moomivand, 2020, Effect of infill material of discontinuities on the failure criterion of rock under triaxial compressive stresses: Theoretical and Applied Fracture Mechanics, **108**, 102652, doi: 10.1016/j.tafmec.2020.102652.

Mousavi, S. Z. S., H. Tavakoli, P. Moarefvand, and M. Rezaei, 2019, Assessing the effect of freezing-thawing cycles on the results of the triaxial compressive strength test for calc-schist rock: International Journal of Rock Mechanics and Mining Sciences, **123**, 104090, doi: 10.1016/j.ijrmms.2019.104090.

Pedersen, S. I., and T. Skov, 2002, Automatic fault extraction using artificial ants: 72nd Annual International Meeting, SEG, Expanded Abstracts, 512–515, doi: 10.1190/1.1817297.

Ren, H. L., C. L. Liu, W. P. Liu, X. Y. Yang, and W. Y. Li, 2020, Stress field simulation and fracture development prediction of the Wufeng Formation-Longmaxi Formation in the Fushun-Yongchuan Block, Sichuan Basin: Journal of Geomechanics, **26**, 74–83.

Shao, X. Z., M. M. Wang, X. Hui, S. M. Wang, X. L. Zhang, and Y. L. Qi, 2021, Characteristics, formation stages and development model of fractures in Yanchi area, Ordos Basin: Natural Gas Geoscience, **32**, 1501–1513.

Su, X. C., L. Gong, S. Gao, X. P. Zhou, Z. S. Wang, and B. Liu, 2021, Characteristics and quantitative prediction of fractures of tight reservoir in Chang 7 member in Longdong area: Xinjiang Petroleum Geology, **42**, 161–167.

Tani, K., T. Nozaki, S. Kaneko, Y. Toyo-Oka, and H. Tachikawa, 2003, Down-hole triaxial test to measure average stress-strain relationship of rock mass: Soils and Foundations, **43**, 53–62, doi: 10.3208/sandf.43.5_53.

Wan, T. F., 1996, Intraplate deformation and tectonic stress field of Mesozoic and Cenozoic in China: Journal of Geomechanics, **03**, 13.

Wang, J. M., and S. Zhang, 2018, Exploring the characteristics and genesis of low amplitude structures on the Yishaan slope, Ordos Basin: Earth Science Frontiers, **25**, 246–253, doi: 10.13745/j.esf.yx.2017-12-27.

Wang, L. J., H. C. Wang, W. Wang, B. S. Sun, and Z. J. Qiao, 2004, Relation among three dimensional tectonic stress field, fracture and migration of oil and gas in oil field: Chinese Journal of Rock Mechanics and Engineering, **23**, 4052–4057.

Wu, L. Q., C. L. Liu, B. Li, and Z. L. Wang, 2018, The application of two factor method in quantitative prediction of tectonic fractures: A case study of shale in Qing-1 member, Songliao Basin: Journal of Geomechanics, **24**, 598–606.

Xu, L. F., Y. S. Cheng, J. C. Zhang, W. Dang, Y. Liu, X. Tang, J. L. Niu, and Z. Z. Tong, 2022, Origin and isotopic fractionation of shale gas from the Shanxi Formation in the southeastern margin of Ordos Basin: Journal of Petroleum Science and Engineering, **208**, 109189, doi: 10.1016/j.petrol.2021.109189.

Yang, H., X. Y. Liu, G. L. Zhang, T. Y. Han, and X. Hui, 2007, The main controlling factors and distribution of low permeability lithologic reservoirs of Triassic Yanchang Formation in Ordos Basin: Lithologic Reservoirs, **19**, 1–6.

Yang, W. L., X. Y. Li, Z. Xu, and E. D. Li, 2019, Shale oil resource assessment for the member Chang7 in Ansai area of Ordos basin: Marine Geology Frontiers, **35**, 48–56.

Zeng, L. B., 2008, Study on the influence of rock heterogeneity on fracture development: Progress in Natural Science, **02**, 216–220.

Zeng, L. B., Z. X. Li, C. E. Shi, Z. G. Wang, J. Y. Zhao, and Y. K. Wang, 2007, Characteristics and origin of fractures in the extra low-permeability sandstone reservoirs of the upper Triassic Yanchang Formation in the Ordos Basin: Acta Geologica Sinica, **81**, 174–180.

Zeng, L. B., and S. R. Xiao, 1999, Fractures in the mudstone of tight reservoirs: Experimental Petroleum Geology, **21**, no. 3, 266–269.

Zeng, L. B., and X. Y. Zhao, 2019, Natural fractures and waterflooding induced fractures in Ordos Basin: Science Press Inc.

Zhang, H., 1996, Mesozoic and cenozoic palaeoteetonostress field of Ordos Basin: Journal of Geology & Mineral Research of North China, **11**, 87–92.

Zhang, H. J., R. G. Wang, X. C. Li, J. Zhuang, C. L. Liu, T. Hou, Z. L. Xu, Q. B. Zang, H. L. Ren, and X. Y. Yang, 2021, Stress field simulation of the Chang 7 Formation in the Ansai, Ordos Basin: Science Technology and Engineering, **21**, 1342–1349.

Zhang, H. J., R. G. Wang, X. C. Li, J. Zhuang, C. L. Liu, T. Hou, Z. L. Xu, Q. B. Zang, K. Wang, H. L. Zhang, R. H. Zhang, J. S. Dai, J. P. Wang, and L. B. Zhao, 2015, Comprehensive assessment of reservoir structural fracture with multiple methods in Keshen-2 gas field, Tarim Basin: Acta Petrolei Sinica, **6**, 673–687, doi: 10.7623/syxb201506004.

Zhao, G., W. L. Ding, Y. X. Sun, X. H. Wang, L. Tian, J. S. Liu, S. Y. Shi, B. C. Jiao, and L. Cui, 2020, Fracture development characteristics and controlling factors for reservoirs in the Lower Silurian Longmaxi Formation marine shale of the Sangzhi block, Hunan Province, China: Journal of Petroleum Science and Engineering, **184**, 106470, doi: 10.1016/j.petrol.2019.106470.

Zhao, G., Z. J. Jin, W. L. Ding, G. X. Liu, J. B. Yun, R. Y. Wang, and G. P. Wang, 2022, Developmental characteristics and formational stages of natural fractures in the Wufeng-Longmaxi Formation in the Sangzhi Block, Hunan Province, China: Insights from fracture cements and fluid inclusions studies: Journal of Petroleum Science and Engineering, **208**, 109407, doi: 10.1016/j.petrol.2021.109407.

Biographies and photographs of the authors are not available.

DOI:10.1190/INT-2021-0181.1